

Characterization of the flow field inside a Ranque-Hilsch vortex tube using filtered Rayleigh scattering, Laser-2-Focus velocimetry and numerical methods

Ulrich Doll^{*,1}, Manfred Beversdorff¹, Guido Stockhausen¹, Christian Willert¹, Daniel Schlüß², Christian Morsbach²

Institute of Propulsion Technology, German Aerospace Center (DLR), 51170 Köln, Germany

1: Department of Engine Measurement Systems

2: Department of Numerical Methods

*correspondent author: ulrich.doll@dlr.de

Abstract The design process of aero engines as well as stationary gas turbines is largely dominated by the cost and time efficient methods of Computational Fluid Dynamics (CFD). Over the past decade the CFD solver TRACE for Favre-averaged compressible Navier-Stokes equations has been developed at the Institute of Propulsion Technology and has been adopted for research as well as industrial applications. In the context of turbomachinery design, reliable modeling of the turbulent flow phenomena involved is a crucial aspect and one of the major subjects of numerical research in fluid dynamics. Novel approaches accounting for the anisotropy of the Reynolds stress tensor promise an improved accuracy in the simulation of industrially relevant configurations. One key aspect in the development strategy of turbulence models is the direct comparison of computational results with validation data produced from appropriate experimental setups with well-defined geometries and boundary conditions. The Ranque-Hilsch vortex tube (RHVT) was chosen in this respect due to its simple geometry with no moving parts on the one hand and its nevertheless complex 3D flow features on the other hand. To provide suitable experimental data the filtered Rayleigh scattering technique extended by the method of frequency scanning (FSM-FRS) was chosen to characterize the RHVT's averaged flow field, since it is capable of simultaneously providing planar information on temperature, pressure and flow field velocity (through the Doppler shift). As the reconstruction of a three component velocity field from FSM-FRS data would require the measurement plane to be observed from three independent directions, the point-wise Laser-2-Focus (L2F) technique is applied to provide 2C velocity profiles at discrete positions downstream from the cold exit.

1. Introduction

The design process of aero engines as well as stationary gas turbines is largely dominated by the cost and time efficient methods of Computational Fluid Dynamics (CFD). Over the past decade the CFD solver TRACE for Favre-averaged compressible Navier-Stokes equations has been developed at the Institute of Propulsion Technology and has since then been adopted for research as well as industrial applications (Becker et al, 2010). In the context of turbomachinery design, reliable modeling of the turbulent flow phenomena involved is a crucial aspect and one of the major subjects of numerical research in fluid dynamics. Novel approaches accounting for the anisotropy of the Reynolds stress tensor promise an improved accuracy in the simulation of industrially relevant configurations (Morsbach et al, 2012). One key aspect in the development strategy of turbulence models is the direct comparison of computational results with validation data produced from appropriate experimental setups with well-defined geometries and boundary conditions. The Ranque-Hilsch vortex tube (RHVT) (Ranque, 1933; Hilsch, 1947) was chosen in this respect due to its simple geometry with no moving parts on the one hand and its nevertheless complex 3D flow features on the other hand.

In the past years, the utilization of advanced numerical methods such as Large Eddy Simulation (LES) or Direct Numerical Simulation (DNS) has become increasingly popular. Still, up to now, the

applicability of these methods to problems of industrial relevance is limited due to their extensive usage of computational resources (Spalart, 2010). For this reason Reynolds-Averaged Navier-Stokes (RANS) methods are still state of the art in commercial applications as well as in industry related research and deliver reliable results.

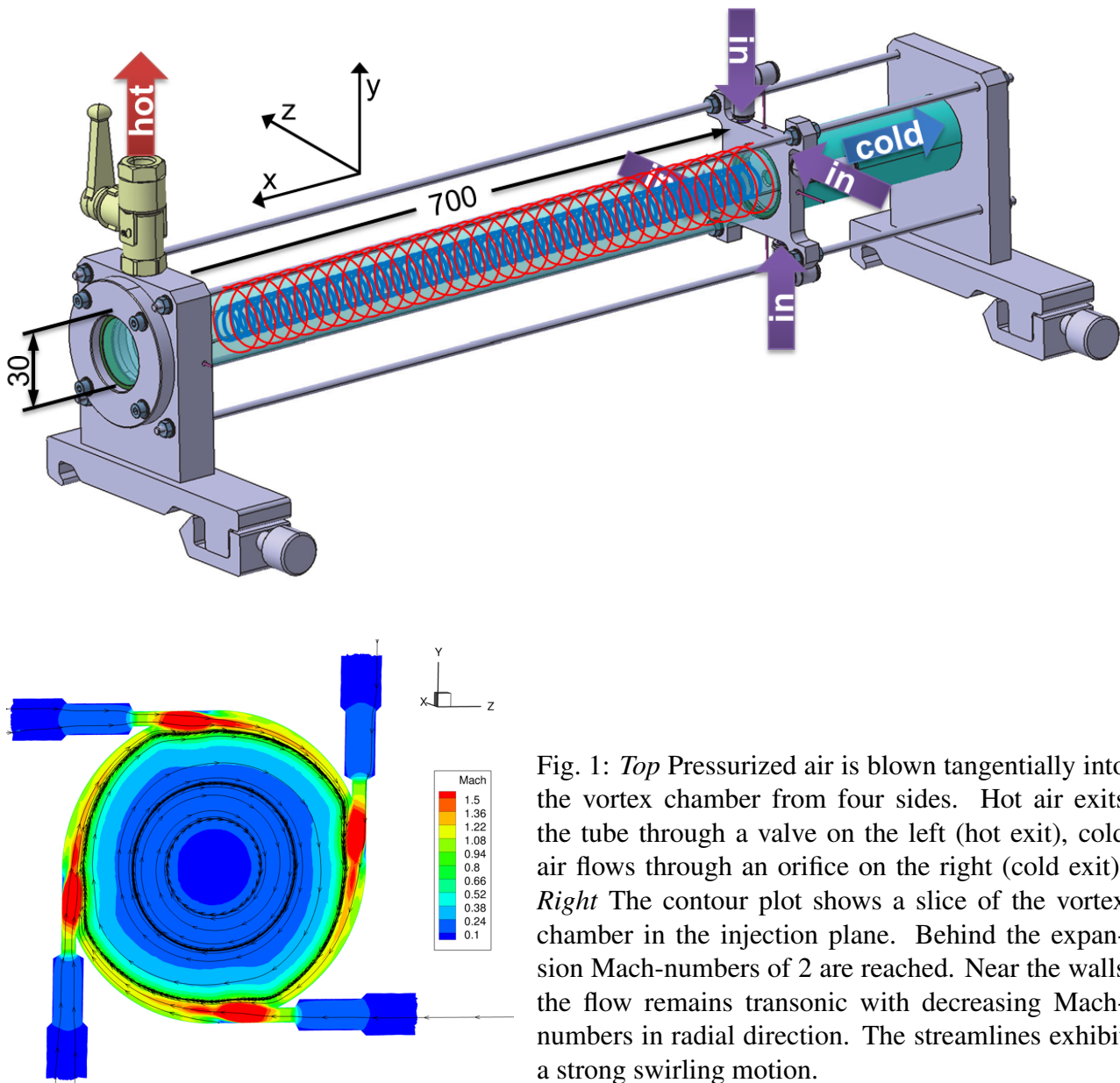


Fig. 1: *Top* Pressurized air is blown tangentially into the vortex chamber from four sides. Hot air exits the tube through a valve on the left (hot exit), cold air flows through an orifice on the right (cold exit). *Right* The contour plot shows a slice of the vortex chamber in the injection plane. Behind the expansion Mach-numbers of 2 are reached. Near the walls the flow remains transonic with decreasing Mach-numbers in radial direction. The streamlines exhibit a strong swirling motion.

In RANS methods the impact of turbulence on the averaged flow field is expressed through the Reynolds stress tensor. For most industrial applications, Linear Eddy Viscosity Models (LEVM) based on Boussinesq's assumption are employed. By nature, these approaches are developed and calibrated for specific flow topologies and may, therefore, fail in more complex flows with anisotropic turbulence fields. To account for anisotropy in turbulence, either transport equations (Differential Reynolds Stress Models DRSM) or algebraic formulations (Explicit Algebraic Reynolds Stress Models EARSM) can be used to model the six independent components of the Reynolds stress tensor (Morsbach et al, 2012). These approaches promise to be more general and should, hence, be able to predict a wider range of possible flow features. In this work, the RHVT's flow field, which is highly three-dimensional involving adiabatic expansion, radial compression, internal friction, turbulent mixing, etc. (Secchiaroli et al, 2009), will be characterized by the Menter SST $k-\omega$ LEVM (Menter et al,

2003) and compared to results calculated with Hellsten EARSM $k-\omega$ (Hellsten, 2005) and SSG/LRR- ω DRSM (Cécora et al, 2012).

Fig. 1, *top*, shows a 3D sketch of the RHVT investigated herein. The main part of the device is a cylindrical tube of 700 mm in length and 30 mm in diameter, made of quartz glass to enable optical access. Pressurized air is blown tangentially into a vortex chamber at the right end of the cylinder from four sides through critical nozzles, which induces a strong swirling motion in the fluid before entering the actual glass tube. Due to energy transfer involving conduction, diffusion and mainly turbulent mixing (Liew et al, 2012) a temperature separation process takes place, leading to higher temperatures in the peripheral region of the tube, while the fluid near the centre of the tube is cooled down. The heated air streams out through a valve on the left, while the cold air leaves the system through an orifice on the right. The flow field can be characterized by the cold fraction $\epsilon = \dot{m}_{cold}/\dot{m}$, being the mass flow ratio of cold air to total air flow. The ratio can be regulated by the valve at the hot exit. The contour plot in Fig. 1, *right*, shows a slice of the vortex chamber in the injection plane. Downstream of the expansion Mach-numbers of 2 are reached. Near the walls the flow remains transonic with decreasing Mach-numbers in radial direction. The streamlines exhibit a strong swirling motion.

Given that the flow inside the vortex tube is purely a fluid dynamical process (Secchiaroli et al, 2009), CFD methods seem predestined to address the not yet fully understood temperature separation process mentioned above. In order to validate the simulation data, time averaged as well as instantaneous measurements of the relevant flow quantities are required. To provide suitable experimental data the filtered Rayleigh scattering technique (Miles and Lempert, 1990) extended by the method of frequency scanning (FSM-FRS) (Forkey et al, 1996; Boguszko and Elliott, 2005; Doll et al, 2014) was chosen to characterize the RHVT's averaged flow field, since it is capable of simultaneously providing planar information on temperature, pressure and flow field velocity (through the Doppler shift). FSM-FRS makes use of the fact, that narrow bandwidth laser light scattered from surfaces (geometric) or large particles (Mie) can be removed from the measured signal by means of molecular absorption, while shares of the spectrally broadened Rayleigh scattering pass through (Fig. 2, *left*) the absorption filter. Molecular iodine was chosen for the absorption filter because it exhibits several appropriate transitions in the vicinity of the 532 nm light emitted by commonly available Nd:YAG laser light sources. In FSM-FRS the laser is tuned to discrete frequencies along the molecular filter's trans-

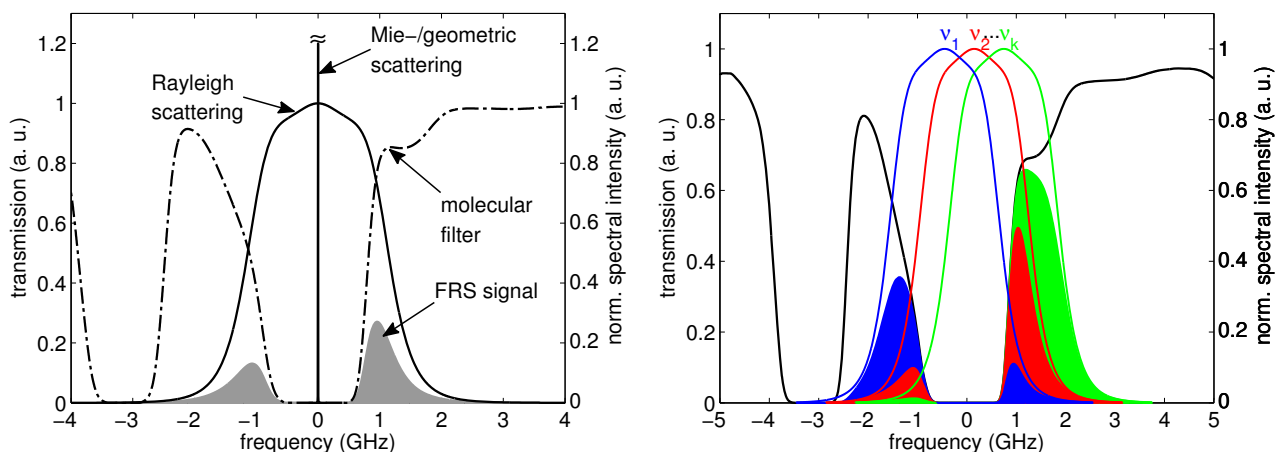


Fig. 2: *Left* Narrow bandwidth light scattered from large particles (Mie) or surfaces (geometric) is filtered, while spectral shares of the Rayleigh scattering pass through. *Right* Frequency scanning method: The laser is modulated multiple times in frequency along the iodine filter's transmission curve.

mission curve. In a stationary process or in time averaged measurements, the Rayleigh scattering's spectral distribution is preserved in shape, while, by shifting the whole spectrum in frequency space, the actual FSM-FRS signal is altered (Fig. 2, right). This results in intensity spectra for each detector element, from which the flow field properties pressure, temperature and Doppler shift can be derived. As the reconstruction of a three component velocity field from FSM-FRS data would require the measurement plane to be observed from three independent directions, the point-wise Laser-2-Focus (L2F) technique (Schodl, 1980), also known as laser transit velocimetry, is applied to provide 2C velocity profiles at discrete positions downstream from the cold exit.

2. Experimental setup and operating conditions

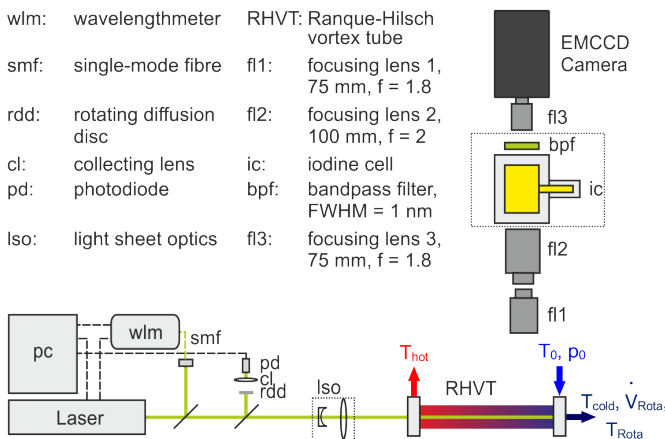


Fig. 3: Principal setup and optical arrangement.

As the FSM-FRS measurements and their comparison to numerical data are the main topics of this contribution and the L2F technique is well established, only an outline of the FSM-FRS setup will be given herein. Fig. 3 shows a schematic sketch of the experimental arrangement. The system is based on a Coherent Verdi V5 continuous wave diodepumped solid state frequency-doubled Nd: YVO₄ laser, emitting single-frequency light at 532 nm with an output power of up to 5 W and a bandwidth <5 MHz. The laser's frequency can be modified by heating or cooling an intra-cavity etalon or by issuing a control voltage on two piezoelectric elements and thus altering the resonator's length. The frequency is monitored and controlled by a High Finesse WSU 10 wavelength meter, which has an absolute accuracy of 10 MHz and allows, by issuing a control voltage on one of the piezos, for a stabilization of the laser's output frequency within ~ 2 MHz of the setpoint. A second control loop accounts for thermal effects in the laser's resonator and ensures long-term frequency stability. As the FSM-FRS signal intensities depend on the incident laser energy, the power has to be monitored throughout the measurement. By putting a thin glass plate into the main beam, a small amount of laser light is directed onto a rotating diffusion disc, in order to produce a homogeneous and structureless intensity distribution. The light scattered from the disc is collected by a lens and focused onto a photodiode. Thus the laser power can be measured with uncertainties smaller than one percent. The laser light is then formed into a light sheet of ~ 30 mm height and ~ 0.5 mm thickness and, after travelling through the whole RHVT's length, illuminates the measurement plane, starting at the cold exit and extending ~ 40 mm in axial direction. The detector unit is oriented perpendicular to polarization and propagation direction of the laser beam to maximize the Rayleigh scattered intensity (Miles et al, 2001). The scattered radiation is collected by a first focusing lens and enters the transfer optics, which is composed of two additional focusing lenses in retro position. In between, the molecular iodine filter cell as well as a bandpass filter (FWHM 1 nm) are placed. Light exiting the filter array is then accumulated by Hamamatsu C9100-13 EM-CCD camera.

In order to adjust and monitor the RHVT's operating conditions, the device is instrumented with several thermocouples, pressure probes and a Rotameter. The inflowing air's pressure p_0 and temperature T_0 are measured at the tube's inlet just before entering the swirl generator. Additionally, temperatures are gathered at the hot (T_{hot}) and the cold (T_{cold}) exits. To adjust the cold fraction ϵ , a valve located downstream from the hot exit can be used. To reach a certain value of ϵ , the desired mass flow rate at the cold exit has to be calculated from the total mass flow rate. \dot{m}_{cold} is then modified by opening or

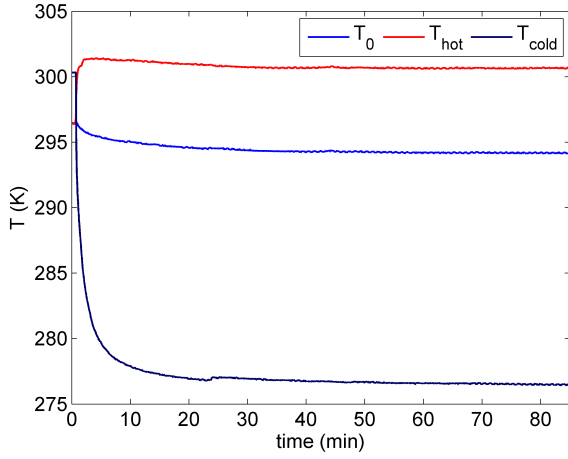


Fig. 4: Time series of thermocouple measurements: T_0 , T_{hot} and T_{cold} are monitored throughout the test. After ~ 30 minutes all temperatures are stable and the FSM-FRS data acquisition starts.

closing the valve at the hot exit until the corresponding value of $\dot{V}_{Rotameter}$ at the Rotameter is reached. Based on the entry conditions chosen for the CFD simulations, the vortex tube was operated with pressurized air at $p_0=7114.7$ hPa. The total mass flow was then 11 g/s (2.75 g/s per entry nozzle) accordingly; the cold fraction was set to 0.3. Fig. 4 shows a time series plot of temperatures measured at the inlet (blue), the hot exit (red) and the cold exit (dark blue). After ~ 30 minutes all temperatures are stable with averaged values for $T_0=294.2$ K, $T_{hot}=300.7$ K and $T_{cold}=277.6$ K, resulting in a ΔT of 24.1 K between hot and cold exit. After the temperatures are stable the standard deviations lie below 0.2 K for all three temperature values.

3. Measurement results and comparison to numerical data

3.1 Data evaluation methodology

The FSM-FRS signal intensities per pixel element ij gathered by the detector can be described by the following expression (Forkey et al, 1996; Boguszko and Elliott, 2005; Doll et al, 2014):

$$S_{ijk}(X, Y, \nu_{0,k}) = R_{ij}I_0 \left(n_{ij}\sigma \left[\int_{-\infty}^{\infty} r_{ij}(X, Y)\tau(\nu + \Delta\nu_{ij})d\nu \right]_k + B_{0,ij}\tau(\nu_{0,k}) + \dots \right. \\ \left. B_{ij}\tau(\nu_{0,k} + \Delta\nu_{ij}) + C_{t,ij} \right) + C_{ij}. \quad (1)$$

The laser's output frequency is tuned in discrete steps along the molecular filter's transmission curve (see Fig. 2, *Right*), which is denoted by the subscript k . The overall intensity per pixel element S_{ijk} at each frequency $\nu_{0,k}$ is comprised of several contributions. The first term in parentheses on the right hand side represents the FRS intensity. n_{ij} , the number density, and σ , the Rayleigh scattering cross section of the investigated gas, are multiplied by the convolution of the Rayleigh scattering's spectral distribution r_{ij} with the molecular filters transmission profile τ . X and Y are input parameters of the Rayleigh scattering's lineshape model by (Tenti et al, 1974). They incorporate the dependencies of the Rayleigh scattering's spectral distribution to pressure p as well as temperature T . $\Delta\nu_{ij}$ is the Doppler shift arising from flow velocity. The second term on the right represents elastic stray light scattered from surfaces such as walls and windows or from large particles at rest (Mie scattering) through the experimental parameter $B_{0,ij}$. Accordingly, the third expression incorporates light scattered from particles travelling with the flow, which is also Doppler shifted by $\Delta\nu_{ij}$, through B_{ij} . $C_{t,ij}$ denotes for background light produced inside the transfer optics of the camera system. While travelling through the optical array, portions of the light collected by the front lens are scattered from glass surfaces and form a background signal, which depends on the structure of the intensity distribution

in the measurement plane. All expressions in parentheses have to be multiplied by an experimental parameter R_{ij} , which describes the optical setup's efficiency and the incident laser intensity I_0 . The parameter C_{ij} represents miscellaneous background contributions such as camera offset.

In order to extract the flow field information on pressure, temperature and Doppler shift from the measured signal, the approach to reduce the number of unknowns of Eq. (1) as described in (Doll et al, 2012, 2014) is applied. In restraining the scanning frequencies to values where the transmission of the molecular filter lies below 10^{-5} , both terms representing the elastically scattered stray light can be neglected. The value of C_{ij} can be easily determined when the laser is shuttered and is subtracted from the measured signal. Thus, Eq. (1) becomes

$$S_{ijk}(X, Y, \nu_{0,k}) = R_{ij}I_0 \left(n_{ij}\sigma \left[\int_{-\infty}^{\infty} r_{ij}(X, Y)\tau(\nu + \Delta\nu_{ij})d\nu \right]_k + C_{t,ij} \right). \quad (2)$$

The standard procedure would now be to determine R_{ij} and $C_{t,ij}$ from a reference frequency scan with pressure and temperature known and zero flow velocity. These values would then be used to evaluate data gathered under operating conditions in order to minimize uncertainties in p , T and $\Delta\nu$.

Fig. 5 shows two raw data images. Both frames display coinciding regions of interest. Fig. 5, *left* was taken at a wave number of 18788.45 cm^{-1} under reference conditions, whereas Fig. 5, *right* was acquired at the same wave number under operating conditions. Despite minor artefacts produced by the light sheet optics and the entry window, the left image exhibits a smooth intensity distribution across the entire imaging region. In contrast, the right image exhibits strong intensity gradients, mainly in the upper and lower regions near the walls and at y -positions of -5 and 5 mm. While changes near the walls are related to flow field phenomena in the measurement plane, the intensity increase at $y = \pm 5$ mm and reduction near the centre of the tube cannot be explained on fluid mechanical grounds. The cause is believed to be related to effects of refractive index variations across the vortex tube. As the laser light sheet travels through the whole extent of the vortex tube to illuminate the measurement plane near the cold exit it is thus exposed to these gradients over a long distance and a considerable amount of light is deflected. The effect is clearly visible in Fig. 5 *left*, where the intersection zones at $y = -5$ mm and $y = 5$ mm appear as bright thin layers, while the intensity drops to the tube's centre. As the FSM-FRS technique is intensity based, a change in the

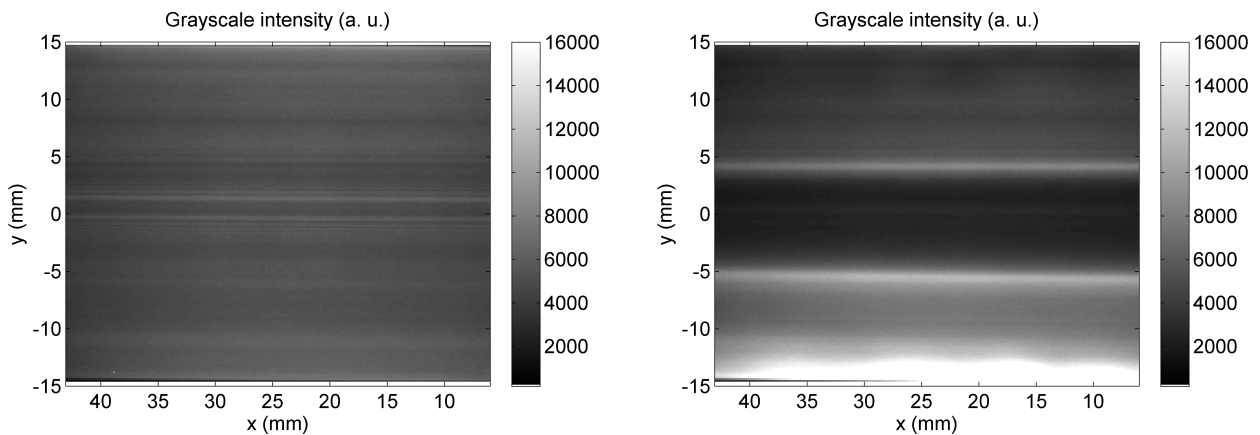


Fig. 5: *Left* Raw data image from the reference frequency scan taken at a wave number of 18788.45 cm^{-1} . *Right* Raw data image from the frequency scan under operating conditions taken at the same wave number.

intensity distribution from reference to operating conditions will result in misinterpreted data, leading to large deviations in pressure, temperature and Doppler shift.

As mentioned earlier in this section, the intensity structure of the light sheet determines the distribution of R_{ij} and $C_{t,ij}$ in the measurement plane and therefore their values must change from reference to operating conditions. The data evaluation is based on a non-linear Levenberg-Marquardt regression method. In fitting the model equation to measured data, the algorithm tries to minimize the residuals between model and data in a least-squares sense. As the best-fit set of parameters only represents a local minimum in a multi-dimensional parameter space, the effort to find a physically reasonable solution rises with the number of unknowns (Vetterling et al, 1992). As R_{ij} is connected linearly to both terms of Eq. (2), fitting this parameter will have a large impact on measurement uncertainties. A possible solution lies in a normalization approach. In dividing the overall intensity S_{ijk} by its ensemble average $\langle S_{ij} \rangle$, the resulting model equation

$$Q_{ijk}(X, Y, \nu_{0,k}) = \frac{S_{ijk}}{\langle S_{ij} \rangle} = \frac{n_{ij} \left[\int_{-\infty}^{\infty} r_{ij}(X, Y) \tau(\nu + \Delta\nu_{ij}) d\nu \right]_k + C_{t,ij}}{n_{ij} \frac{1}{K} \sum_{k=1}^K \left[\int_{-\infty}^{\infty} r_{ij}(X, Y) \tau(\nu + \Delta\nu_{ij}) d\nu \right]_k + C_{t,ij}} \quad (3)$$

is independent of the experimental parameter R_{ij} . In the following, this expression will be used in the fitting routine to process the FSM-FRS measurement data.

3.2 Results

All numerical and experimental results shown in this section are related to the operating conditions described in Sect. 2. During the FSM-FRS experiments, the camera was operated in CCD-mode with 2 x 2 hardware binning, resulting in 256 x 256 pixel elements with a resolution of 0.15 mm/pixel. The exposure time was set to 5 s for all scanning frequencies. The distance between two successive frequency values was ~ 30 MHz, resulting in a total number of 58 scanning frequencies. The evaluated data set is averaged over 5 consecutive runs, leading to a total measurement time of about one hour.

Fig. 6 shows a comparison of pressure, temperature and Doppler shift maps, calculated by the Menter SST $k-\omega$ turbulence model ((a), (c), (e)) and measured by FSM-FRS ((b), (d), (f)). The y -coordinate resembles the diameter of the RHVT's cross section, while the x -coordinate begins 6 mm from the injection plane and extends about 36 mm downstream. The simulated pressure map of Fig. 6a exhibits a nearly constant distribution in the core region and, beginning at $y = \pm 10$ mm, rises from ambient pressure about 300 hPa towards the tube's walls. The pressure map determined from FSM-FRS (Fig. 6b) instead is rather chaotic and exhibits artefacts resembling the light sheets intensity distribution as displayed in Fig. 5 right. Comparing the two temperature maps of Fig. 6c and Fig. 6d, they qualitatively present similar structures, with cold temperatures near 240 K in the upper and lower right corners, where the transonic tangential air injection governs the flow. Its influence is more pronounced in the measured data and exhibits a slight asymmetry. The zones of lowered temperature at the RHVT's boundary reaches from $x = 6$ mm to $x = 35$ mm in axial direction for the simulated data and extends even further to $x = 42$ mm for the measured temperature distribution. Moving from the tube's edge toward the centre, at a radial position of $y = \pm 10$ mm, the temperature rises abruptly by ~ 10 K and subsequently stabilizes to a nearly constant value. Whereas the qualitative agreement between simulation and measurement is good, on average, temperatures calculated with the Menter SST $k-\omega$ model lie about 10 K above the measured values. Fig. 6e and Fig. 6f show a comparison of Doppler shift maps calculated from the three component velocity distribution obtained by CFD according to the scattering geometry and measured by FSM-FRS. Comparing the two distributions,

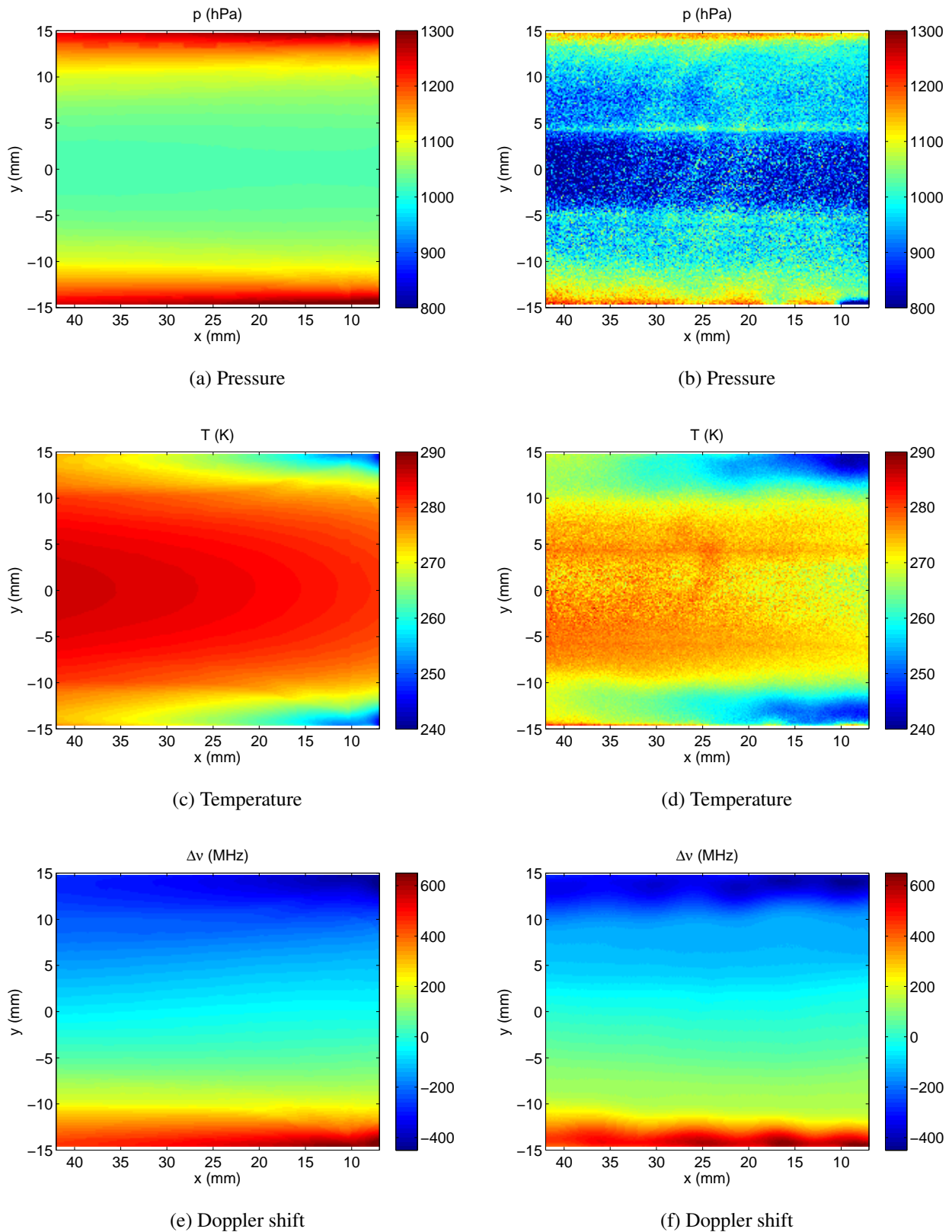


Fig. 6: Comparison of pressure, temperature and Doppler shift maps. (a), (c) and (e) show p , T and $\Delta\nu$ of the averaged flow field calculated by the Menter SST k - ω turbulence model. (b), (d) and (f) present the corresponding FSM-FRS results.

there is good agreement in absolute values ranging from +650 MHz to –450 MHz (corresponding to an absolute velocity of ± 250 m/s) as well as in topology. Again both maps show the influence of the transonic tangential air injection as zones of heightened $\Delta\nu$ near the injection plane, until the flow homogenizes with increased axial distance. Whereas in CFD Doppler shift data the zones of heightened $\Delta\nu$ extend evenly about 5 mm from the tube’s boundary into the flow for all axial positions, in the measured data, these zones are less pronounced near the tangential air injection and expand radially with the flow travelling downstream in axial direction. The associated gradient reveals a wave like structure for the measurements, while the CFD shows a smooth distribution.

In order to compare CFD results of the three different turbulence models and the data gathered by FSM-FRS and L2F measurements, radial profiles of pressure (Fig. 7), temperature (Fig. 8) and Doppler shift (Fig. 9) at three axial positions are plotted with respect to each other. In Fig. 7, pressure profiles are shown for Menter SST $k-\omega$ (blue), Hellsten EARSM $k-\omega$ (black), SSG/LRR- ω (green) and FSM-FRS measurements (red) at axial positions of $x = 7$ mm (*Left*), $x = 14$ mm (*Middle*) and $x = 35$ mm (*Right*). Both the Menter SST $k-\omega$ and Hellsten EARSM $k-\omega$ models show a similar pattern throughout the tube’s cross section for all axial positions. Bearing merely the same values in the core region, both pressures curves increase towards the tube’s boundary, whereas the gradient is steeper in case of the Menter SST $k-\omega$. With increasing axial distance, the starting point of the pressure rise is slightly shifted towards the core region. In case of the SSG/LRR- ω model, the zone of constant pressure is further extending in radial direction, followed by a steep gradient, beginning ~ 2 mm off the wall. As the pressure rise is shifted towards the tube’s boundary, the predicted absolute values of SSG/LRR- ω lie below Menter SST $k-\omega$ and Hellsten EARSM $k-\omega$. In the core region, all three turbulence models show similar results. As stated earlier, the FSM-FRS pressure results exhibit strong noise. On average, the CFD data shows higher absolute values at the tube’s core region as well as at it’s boundary. Whereas in Fig. 7 *left* due to the low quality of the measurement results no valid statement can be given, the FSM-FRS pressure profiles at $x = 14$ mm and $x = 35$ mm exhibit similar patterns compared to Menter SST $k-\omega$ and Hellsten EARSM $k-\omega$ models.

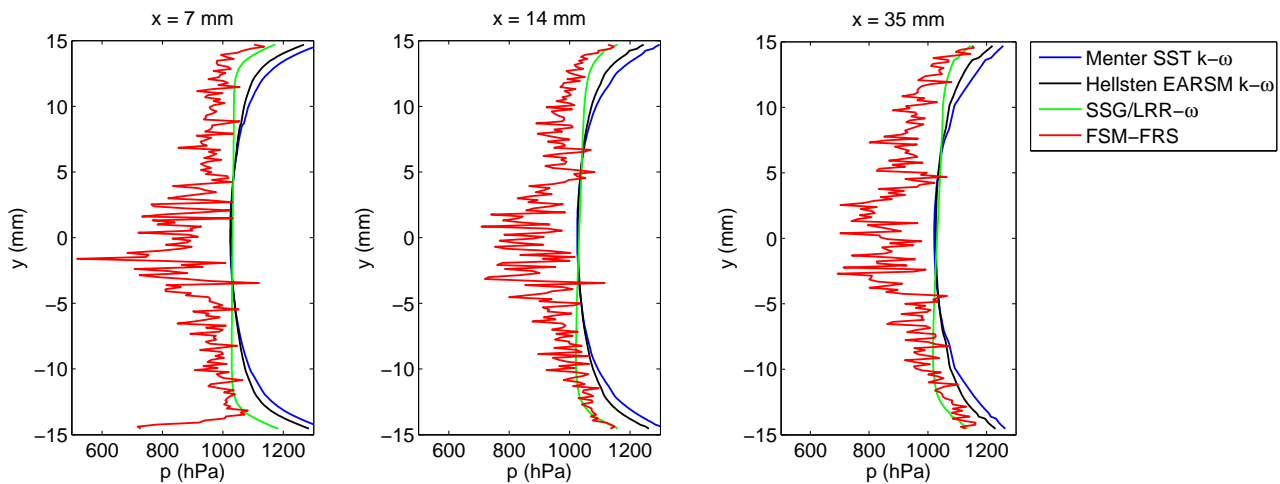


Fig. 7: Comparison of pressure profiles at $x = 7$ mm (*Left*), $x = 14$ mm (*Middle*), $x = 35$ mm (*Right*).

In Fig. 8 temperature profiles computed by the three different turbulence models and FSM-FRS results are plotted against each other. In the tube’s core region, all three turbulence models predict higher temperatures than measured. When moving towards the boundary, for axial positions at $x = 7$ mm and $x = 14$ mm, the SSG/LRR- ω is in good agreement to FSM-FRS results. Menter SST $k-\omega$ and Hellsten EARSM $k-\omega$ models again show similar patterns. Compared to FSM-FRS measurements and SSG/LRR- ω turbulence model, the region of higher temperatures in the tube’s core region is more pronounced using these models, with steeper gradients towards the walls. The turning point

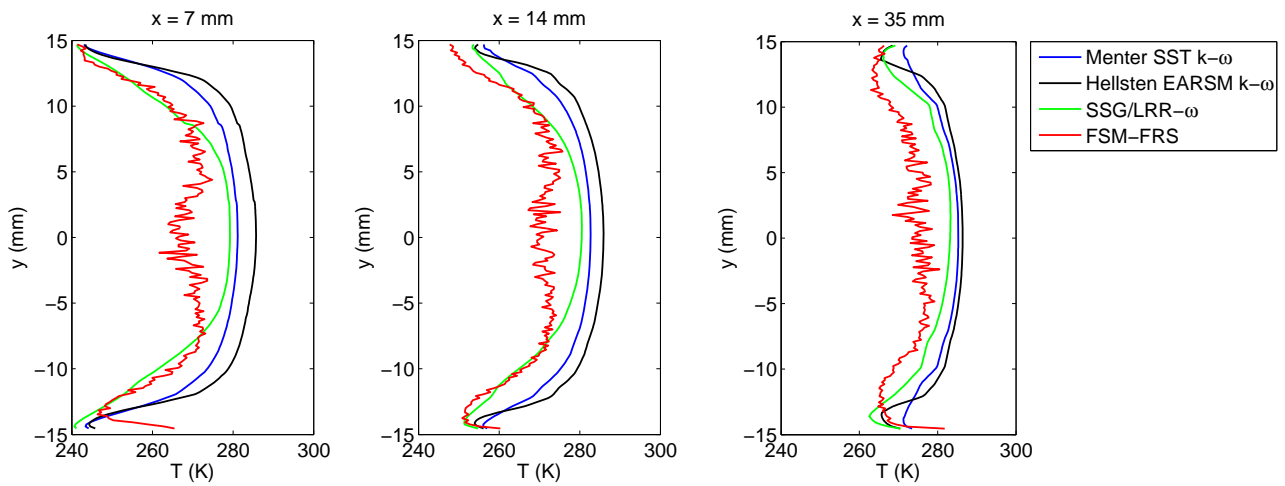


Fig. 8: Comparison of temperature profiles at $x = 7$ mm (Left), $x = 14$ mm (Middle), $x = 35$ mm (Right).

in FSM-FRS results at the tube's boundary near $y = -15$ mm in Fig. 8 middle and Fig. 8 right is predicted by all models. The agreement between SSG/LRR- ω and measured results at an axial position of $x = 14$ mm is very well in both shape and magnitude. At an axial position $x = 35$ mm, calculated curves as well as measured profile exhibit an "S" pattern with temperatures decreasing beyond $y = \pm 8$ mm and then increasing again towards the tube's upper and lower boundary. In all calculated curves the structure is differently pronounced. The Menter SST $k-\omega$ model shows, despite higher absolute values of about 10 K, the best qualitative agreement to the measured data.

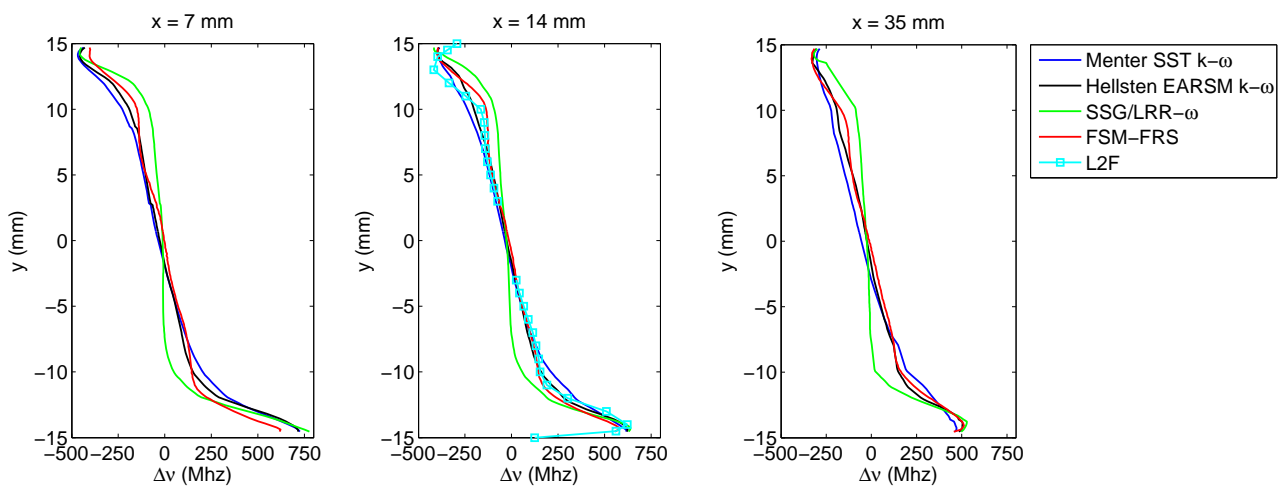


Fig. 9: Comparison of Doppler shift profiles at $x = 7$ mm (Left), $x = 14$ mm (Middle), $x = 35$ mm (Right). At an axial position of $x = 14$ mm, corresponding Doppler shift values calculated from L2F data are included.

Fig. 9 shows Doppler shift profiles calculated from simulated flow velocity and measured by FSM-FRS for the three axial positions. Additionally, a radial two component velocity profile, covering x - and z -directions, was gathered by L2F at $x = 14$ mm, which is converted to Doppler shift frequencies as well. In the tube's core region no reliable L2F data could be acquired due to insufficient seeding density. Menter SST $k-\omega$ and Hellsten EARSM $k-\omega$ models show, especially in the tube's core region, the best agreement to the measured data in absolute value as well as in shape, whereas the SSG/LRR- ω model exhibits large deviations. When moving in radial direction towards the tube's boundaries, the

tangential velocity component becomes dominant around $y = \pm 10$ mm, resulting in a steep Doppler shift gradient towards the wall. The effect is strongest at an axial position of $x = 7$ mm near the tangential injection plane and declines with increasing axial distance. In Fig. 9 *left* the zones of high absolute Doppler shift values predicted by Menter SST $k-\omega$ and Hellsten EARSM $k-\omega$ models further extend in radial direction and exhibit higher peak values compared to the corresponding FSM-FRS curve. At an axial position of $x = 14$ mm, data measured by FSM-FRS and L2F show excellent agreement in the tube's lower half, where shape as well as absolute value are matched. In this region, the Hellsten EARSM $k-\omega$ agrees very well with the measured data and shows only slight deviations. In the upper half, L2F and FSM-FRS curves present a similar pattern, drawing an "S"-shape beginning at $y = 7$ mm, whereas the effect is more pronounced in the L2F profile. At $x = 35$ mm, Hellsten EARSM $k-\omega$ calculation and FSM-FRS data show the best agreement, while the still persistent "S"-shape in the tube's upper half is not resolved by CFD methods.

4. Discussion

In the previous section, measurement results acquired with FSM-FRS and L2F techniques are compared to numerical data, calculated by the use of three different turbulence modelling approaches. As a detailed discussion of similarities and differences between simulation and experiment, especially on the numerical side, would go beyond the scope of this study, mainly aspects concerning the FSM-FRS measurements will be discussed in this section.

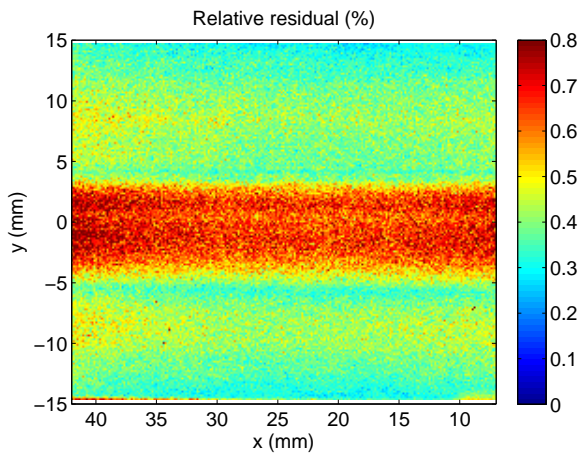


Fig. 10: Distribution of relative residuals of the $pT\Delta\nu C_t$ data fit.

While temperature and Doppler shift results are of good quality and resemble the expected structure of the flow field, the pressure distribution exhibits an elevated noise level, which gets even higher in the tube's core region. In this context it seems appropriate to assess the limits of uncertainty of the FSM-FRS measurement results. In Fig. 10 the distribution of the relative residual of the $pT\Delta\nu C_t$ data fit is presented. The relative residual map can be interpreted as a measure of data quality for each camera pixel element. While from the tube's boundary until y -positions of ± 5 mm the residuals lie between 0.3 and 0.5 %, in the poorly illuminated core region these values double. To assess the uncertainties

	p (hPa)	T (K)	$\Delta\nu$ (MHz)
outer region	30	1	1
core region	70	2	2

Tab. 1: Estimated uncertainties for pressure, temperature and Doppler shift in the tube's outer zone and core region

for pressure, temperature and Doppler shift, as described in (Doll et al, 2014), a simulated FSM-FRS data set resembling the characteristics of the investigated flow is generated. After adding Gaussian noise, the fitting algorithm is repeated 100 times in order to recover the original parameter set. The amplitude of the Gaussian noise is chosen as such, that it matches the relative residuals' values in the outer zone as well as in the core region. The results of the analysis are summarized in Table 1. The uncertainties lie between 30 to 70 hPa for pressure, 1 to 2 K for temperature and 1 to 2 MHz for Doppler shift for outer and core region respectively.

On a relative scale, the uncertainties in pressure amount up to 7 %, whereas the uncertainties of temperature and Doppler shift, are well below 2 %. An explanation lies in the normalization procedure described in Sect. 3.1 As a significant amount of sensitivity of the FSM-FRS signal to pressure is due to the number density, in dividing the overall intensity by it's ensemble average, the influence of n on the signal is severely reduced and pressure sensitivity is only generated from associated changes in the Rayleigh scatterings spectral lineshape.

While the general agreement between numerical data and measurement results is good, each model has it's strength and flaws. Despite the low quality of the FSM-FRS pressure data, qualitatively, Menter SST $k-\omega$ and Hellsten EARSM $k-\omega$ profiles of Fig. 7 *middle* and *right* are similar in shape compared to the measured pressure curves. In Fig. 8 *left* and *middle* instead, the temperature in the tube's outer region is reflected by the SSG/LRR- ω turbulence model, while in Fig. 8 *right* the Menter SST $k-\omega$ exhibits the best qualitative agreement. Despite the "S"-shape, visible in FSM-FRS as well as L2F results, the Hellsten EARSM $k-\omega$ shows very good agreement in Doppler shift.

5. Conclusion

The flow field in a Ranque-Hilsch vortex tube was characterized by means of numerical simulations, including three different turbulence models, planar measurements using the frequency scanning filtered Rayleigh scattering technique and point wise measurements using the Laser-2-Focus technique. The turbulence models used in CFD calculations were the Menter SST $k-\omega$ LEVM, the Hellsten EARSM $k-\omega$ and the SSG/LRR- ω DRSM. Numerical results were compared to averaged pressure, temperature and Doppler shift data gathered with FSM-FRS and a velocity profile acquired by L2F. Because the light sheet's intensity distribution is altering between reference and operating conditions, a novel methodology for the evaluation of FSM-FRS data was introduced. In normalizing the overall signal intensity by it's ensemble average, the resulting data becomes almost invariant to changes in the intensity distribution. The uncertainties of the method were assessed to lie below 70 hPa, 2 K and 2 MHz for pressure, temperature and Doppler shift, respectively.

Concerning the numerical simulations, the results of FSM-FRS and L2F measurements can be used to further enhance the existing turbulence modelling approaches. It was shown that the FSM-FRS technique, by delivering high quality validation data, can contribute in the improvement of sophisticated CFD methods.

References

- Becker K, Heitkamp K, Kügeler E (2010) Recent progress in a hybrid-grid cfd solver for turbomachinery flows. In: V European Conference on Computational Fluid Dynamics ECCOMAS CFD 2010, Lisbon, Portugal
- Boguszko M, Elliott G (2005) On the use of filtered rayleigh scattering for measurements in compressible flows and thermal fields. *Experiments in Fluids* 38(1):33–49
- Cécora RD, Eisfeld B, Probst A, Crippa S, Radespiel R (2012) Differential reynolds stress modeling for aeronautics. In: 50th AIAA Aerospace Sciences Meeting, Nashville, TN, USA
- Doll U, Fischer M, Stockhausen G, Willert CE (2012) Frequency scanning filtered rayleigh scatter-

- ing in combustion experiments. In: 16th Int Symp on Applications of Laser Techniques to Fluid Mechanics, The International Symposia on Applications of Laser Techniques to Fluid Mechanics
- Doll U, Stockhausen G, Willert C (2014) Endoscopic filtered rayleigh scattering for the analysis of ducted gas flows. *Experiments in Fluids* 55(3):1–13, DOI 10.1007/s00348-014-1690-z, URL <http://dx.doi.org/10.1007/s00348-014-1690-z>
- Forkey J, Finkelstein N, Lempert W, Miles R (1996) Demonstration and characterization of filtered rayleigh scattering for planar velocity measurements: Aerodynamic measurement technology. *AIAA journal* 34(3):442–448
- Hellsten A (2005) New advanced k - ω turbulence model for high-lift aerodynamics. *AIAA J* 43(9):1857–1869
- Hilsch R (1947) The use of the expansion of gases in a centrifugal field as cooling process. *Review of Scientific Instruments* 18(2):108–113, DOI <http://dx.doi.org/10.1063/1.1740893>, URL <http://scitation.aip.org/content/aip/journal/rsi/18/2/10.1063/1.1740893>
- Liew R, Zeegers J, Kuerten J, Michalek W (2012) Maxwell’s demon in the ranque-hilsch vortex tube. *Physical Review Letters* 109(5), URL <http://www.scopus.com/inward/record.url?eid=2-s2.0-84864488947&partnerID=40&md5=25be79e6c159cca80e4e620036da31a4>, cited By (since 1996)3
- Menter F, Kuntz M, Langtry R (2003) Ten years of industrial experience with the sst model. In: Hanjalić K, Nagano Y, Tummers M (eds) *Turbulence, Heat and Mass Transfer 4*
- Miles R, Lempert W (1990) Two-dimensional measurement of density, velocity, and temperature in turbulent high-speed air flows by uv rayleigh scattering. *Applied Physics B: Lasers and Optics* 51:1–7, URL <http://dx.doi.org/10.1007/BF00332317>, 10.1007/BF00332317
- Miles RB, Lempert WR, Forkey JN (2001) Laser rayleigh scattering. *Measurement Science and Technology* 12(5):R33, URL <http://stacks.iop.org/0957-0233/12/i=5/a=201>
- Morsbach C, Franke M, di Mare F (2012) Towards the application of reynolds stress transport models to 3d turbomachinery flows. In: 7th International Symposium on Turbulence, Heat and Mass Transfer, Palermo, Sicily, Italy
- Ranque GJ (1933) Expériences sur la détente giratoire avec productions simultanées d’un echappement d’air chaud et d’un echappement d’air froid. *Journal de Physique et Le Radium* 4(7):112–114
- Schodl R (1980) A laser-two-focus (12f) velocimeter for automatic flow vector measurements in the rotating components of turbomachines. *Journal of Fluids Engineering, Transactions of the ASME* 102(4):412–419, cited By (since 1996)10
- Secchiaroli A, Ricci R, Montelpare S, D’Alessandro V (2009) Numerical simulation of turbulent flow in a ranque-hilsch vortex tube. *International Journal of Heat and Mass Transfer* 52(23-24):5496–5511, DOI 10.1016/j.ijheatmasstransfer.2009.05.031, URL <http://www.scopus.com/inward/record.url?eid=2-s2.0-69949092816&partnerID=40&md5=0fdf95e5eb9398b6fde298fff7aed211>, cited By (since 1996)22
- Spalart P (2010) Reflections on rans modelling. In: Peng SH, Doerffer P, Haase W (eds) *Progress in Hybrid RANS-LES Modelling, Notes on Numerical Fluid Mechanics and Multidisciplinary Design*, vol 111, Springer Berlin Heidelberg, pp 7–24, DOI 10.1007/978-3-642-14168-3_2, URL http://dx.doi.org/10.1007/978-3-642-14168-3_2
- Tenti G, Boley C, Desai R (1974) On the kinetic model description of rayleigh-brillouin scattering from molecular gases. *Canadian Journal of Physics* 52(4):285–290
- Vetterling W, Flannery B, Press W, Teukolski S (1992) *Numerical Recipes in Fortran-The art of scientific computing*. Cambridge University Press